

Lithiated Prussian blue analogues as positive electrode active materials for stable non-aqueous lithium-ion batteries

Received: 14 November 2021

Accepted: 29 November 2022

Published online: 16 December 2022

Check for updates

Ziheng Zhang^{1,2}, Maxim Avdeev³, Huaican Chen^{4,5}, Wen Yin^{4,5},
Wang Hay Kan^{4,5} & Guang He^{1,6}

Prussian blue analogues (PBAs) are appealing active materials for post-lithium electrochemical energy storage. However, PBAs are not generally suitable for non-aqueous Li-ion storage due to their instability upon prolonged cycling. Herein, we assess the feasibility of PBAs with various lithium content for non-aqueous Li-ion storage. We determine the crystal structure of the lithiated PBAs via neutron powder diffraction measurements and investigate the influence of water on structural stability and Li-ion migration through operando X-ray diffraction measurements and bond valence simulations. Furthermore, we demonstrate that a positive electrode containing $\text{Li}_{2-x}\text{FeFe}(\text{CN})_6 \cdot n\text{H}_2\text{O}$ ($0 \leq x \leq 2$) active material coupled with a Li metal electrode and a LiPF_6 -containing organic-based electrolyte in coin cell configuration delivers an initial discharge capacity of 142 mAh g^{-1} at 19 mA g^{-1} and a discharge capacity retention of 80.7% after 1000 cycles at 1.9 A g^{-1} . By replacing the lithium metal with a graphite-based negative electrode, we also report a coin cell capable of cycling for more than 370 cycles at 190 mA g^{-1} with a stable discharge capacity of about 105 mAh g^{-1} and a discharge capacity retention of 98% at 25°C .

Non-aqueous lithium-ion batteries (LIBs) have become a dominant power source for portable electronic devices, power tools, electric vehicles, and other renewable energy storage systems¹. Albeit its popularity, the thermal runaway induced accidents are occasionally happened all over the world^{2,3}. In commercialized lithium-ion batteries, the layered transition-metal (TM) oxides, represented by a general formula of LiMO_2 , have been widely used as higher energy density positive electrode materials due to their appealing electrochemical performance namely the specific gravimetric capacity, rate capacity and energy density^{4,5}. However, the inadequate thermal stability of the cell at charge states seems inevitable for such

layered structures due to their O $2p$ and M $3d$ orbital overlapping. Consequently, prolonged cycling might induce undesired structural defects of cationic migration and oxide-ion vacancy. Alternatively, polyanion-type cathodes such as LiFePO_4 demonstrate greatly promoted thermal stability due to the strong covalent P–O bonds in the structures^{6–8}. Furthermore, the inductive effect (an electronic effect due to the polarisation of σ bonds within a molecule or ion) brings a higher working potential in polyanion cathodes in comparison to layered lithium metal oxide cathodes. Nonetheless most polyanion cathodes suffer from lower theoretical capacities as compared to their layered counterparts. It's been a

¹Tianjin Key Laboratory of Advanced Functional Porous Materials, Institute for New Energy Materials and Low-Carbon Technologies, School of Materials Science and Engineering, Tianjin University of Technology, Tianjin 300384, China. ²Renewable Energy Conversion and Storage Center (RECAST), Haihe Laboratory of Sustainable Chemical Transformations, Key Laboratory of Advanced Energy Materials Chemistry (Ministry of Education), College of Chemistry, Nankai University, Tianjin 300071, China. ³Australian Nuclear Science and Technology Organization (ANSTO), Lucas Heights, NSW 2234, Australia. ⁴Spallation Neutron Source Science Center, Dalang, Dongguan 523803, China. ⁵Institute of High Energy Physics, Chinese Academy of Sciences, Beijing 100049, China. ⁶Tianneng Co. Ltd, Huzhou 313100, China. e-mail: jianhx@ihep.ac.cn; heguang@tjut.edu.cn

fundamental task to explore new cathode materials for the development of LIBs.

Prussian blue analogues (PBAs) have open channel structure that is suitable for alkali ion de/intercalation, and in certain circumstance two-electron reaction per formula unit could occur with optimized compositions^{9–15}. In the past few years, intercalation behaviors of different metal ions have been studied including Li⁺, Na⁺, K⁺, Rb⁺, NH⁴⁺, Mg²⁺, Zn²⁺ etc., among which Na-PBA is considered the most promising applications in Na-ion batteries (SIBs) with balanced capacities, cell voltages, rate capability and cycling life^{16–19}. For example, the Prussian white Na₂FeFe(CN)₆ has a theoretical capacity of 170 mAh g⁻¹ and average cell discharge voltage of -3 V vs. Na/Na⁺, both of which are competitive among various Na cathodes²⁰. Practically, high discharge capacity (>150 mAh g⁻¹), stable cycling life (>1000 cycles) and good rate capability (>1.9 A g⁻¹) have been demonstrated by research groups in Na-FePBA cells^{21,22}.

Despite the great of PBA materials in SIBs, no commercial SIBs are commercially available yet. On the other hand, the applications of PBA in LIBs are not optimistic due to the following concerns. First, Li intercalation potential is generally higher than for Na in most polyanion frameworks, *i.e.*, FePO₄ and VOPO₄, but this advantage is significantly diminished for Li-PBA cathodes. Furthermore, the replacement of Na ions by Li-ions could cause structural decomposition of PBAs. Goodenough et al. found the shorter Pauli repulsion radius of Li-ion makes it prefer to stay closer to Na as compared to Na in the MnFe(CN)₆ host, which leads to structural evolution of MnN₆ octahedra into LiN₄ and MnN₄ tetrahedra²³. Ling et al. also demonstrate that the stable interstitial site will convert from face-centered site to body-centered site with the ion radius increases²⁴. All these findings suggest the large PBA voids may not match the smaller size of Li-ions.

The PBA framework as the cathode materials for lithium-ion storage was early reported in 1999²⁵, the Fe₄[Fe(CN)₆]₃·5.89H₂O delivered a discharge capacity of 90 mAh g⁻¹ in the first ten cycles at a constant current density of 0.1 mA cm⁻² (lithium coin cells with 1 M LiClO₄ in a propylene carbonate/1,2-dimethoxy ethane as electrolyte, 1:1 vol/vol). After that, there are only few research work using PBAs for lithium insertion such as KMnMn(CN)₆, FeFe(CN)₆^{26–28}. The earliest results demonstrated poor cyclability and practicality of Li-PBA materials. Upon the rise of Na-PBA materials in recent years, there have been much attention on the compositional and structural optimization to attain better performance in SIBs, which is likely to be applied in Li-PBA cathodes. In particular, the two-electron reaction provides very appealing capacities once the M site is rationally designed for the Li₂MFe(CN)₆ cathodes. For example, the Li₂FeFe(CN)₆ has a theoretical capacity of 190 mAh g⁻¹ (*vs.* 170 mAh g⁻¹ for LiFePO₄), even comparable to high-energy layered compounds (LiCoO₂ and LiNi_{0.6}Co_{0.2}Mn_{0.2}O₂). Also, the previous research works indicate less concerns of mass transfer for Na-PBAs, and similar results are expected for Li-PBAs. This is a difference for PBA materials from other Li polyanion cathodes that usually require a nano engineering process before use, because the nanoscale structural design can effectively improve ion or electron diffusion and mitigate the mechanical stress at the cathode side^{29–31}. In terms of the comparison of Li-PBA and Na-PBA, the graphite anode is crucial to boost the energy density in cell-level in LIBs due to the different intercalation potentials between graphite and hard carbon^{10,32}. Supplementary Fig. 1 summarizes the key parameters of lithium-based Prussian blue and other materials, highlighting the necessity to revisit the electrochemical behaviors of tailored PBA cathodes in LIBs, in particular for the water content.

In this work, we prepared lithium-containing Prussian blue hexacyanoferrate materials with different synthetic routes. The structures of samples were determined by powder neutron diffraction, and the dehydration and the chemical degradation process of Li_{2-x}FeFe(CN)₆ (denoted as LiFeHCF) samples were observed by operando variable temperature X-ray diffraction (XRD) and

combined Thermogravimetry-infrared spectrometry (TGA-IR), confirming the influence of zeolitic water in terms of material thermal stability. Compared to other sizes of LiFeHCF samples, the LiFeHCF-1 sample with micron size and single crystal morphology exhibits a high reversible capacity of 142 mAh g⁻¹ at 19 mA g⁻¹. Further electrochemical evaluation shows appealing electrochemical energy storage performance of the LiFeHCF-1 sample under different tests such as high area loading (10 mg cm⁻²), high specific current (1.9 A g⁻¹), long lifespan (over 1000 cycles) and wide temperature windows (-20 °C to 55 °C). The graphite||LiFeHCF-1 coin cell shows the stable cycling life with a capacity retention of 98% after 300 cycles at 25 °C, highlighting the great potentials of Prussian cathodes for practical applications in LIBs.

Results and discussions

Materials synthesis and characterizations

Herein, a series of LiFeHCF samples with different defects and water contents were systemically prepared by different synthetic methods. The specific methods procedures are described in the experimental section. Briefly, LiFeHCF-1, LiFeHCF-2 and LiFeHCF-3 samples were obtained through ion-exchange process, while LiFeHCF-4 and LiFeHCF-5 samples were synthesized through the self-oxidation/precipitation method. Figure 1a shows the schematic illustration of the synthetic route for LiFeHCF-1 by chemical lithiation of FeFe(CN)₆-1 (FeHCF-1), which was first prepared via chemically extracting sodium from NaFeFe(CN)₆-1 (NaFeHCF-1). LiFeHCF-2 and LiFeHCF-3 samples were obtained using NaFeHCF-2 and NaFeHCF-3 as the precursors that were prepared by a citrate-assisted co-precipitation method^{20,22}.

To investigate the chemical desodiation/lithiation process of LiFeHCF-1, LiFeHCF-2 and LiFeHCF-3, the colors of samples at various preparation stages were recorded (Supplementary Fig. 2). Upon the chemical extraction of sodium, the blue NaFeHCF-1 and NaFeHCF-2 were turned to greenish due to the oxidation of Fe²⁺ to Fe³⁺. The blue color was recovered after microwave-assisted treatment with LiI, confirming the chemical intercalation of Li ions into the lattice. The other two LiFeHCF samples LiFeHCF-4 and LiFeHCF-5 were obtained using Li₄Fe(CN)₆ as both Li and Fe source (Supplementary Fig. 3). The XRD patterns confirm all LiFeHCF samples are well crystallized with the cubic structures (Supplementary Fig. 4). TGA (see Supplementary Fig. 5), element analyzer (EA) and inductively coupled plasma mass spectrometry (ICP-MS) (see Supplementary Table 1) were employed to calculate the chemical compositions of different LiFeHCF samples, the results show the LiFeHCF-1, LiFeHCF-2, LiFeHCF-3, LiFeHCF-4 and LiFeHCF-5 samples can be denoted as Li_{1.05}Fe[Fe(CN)₆]_{0.97}□_{0.03}·2.6 H₂O, Li_{1.36}Fe[Fe(CN)₆]_{0.96}□_{0.04}·2.9 H₂O, Li_{1.14}Fe[Fe(CN)₆]_{0.91}□_{0.09}·4.7 H₂O, Li_{0.63}Fe[Fe(CN)₆]_{0.96}□_{0.04}·2.7 H₂O and Li_{1.0}Fe[Fe(CN)₆]_{0.90}□_{0.10}·4.9 H₂O, respectively.

To get the insights of the defect concentration and the location of water molecules, samples were further analyzed by neutron diffraction (Fig. 1b–d, Supplementary Figs. 6 and 7). The long-range ordering of Prussian Blue has been previously studied by Herren, Yusuf and others^{33,34}. We built our initial model based on the Herren research work in which Fe ions are octahedrally coordinated with CN ligands in a cubic structure with a space group of *Fm-3m*. At this stage, no H₂O molecules was put into the unit cell as their locations will be determined by the Fourier-Transform different maps after the initial refinement cycles. Constrain conditions were created such that the molar ratio of Fe and CN was consistent with the ICP result in the investigated samples. Nonetheless, the occupancy parameter was allowed to change, in addition to the parameters associated with profile, cell parameter, thermal factor, background, sample displacement, and transparency. To reduce the number of variables in the refinement, the thermal parameters of C and N were assumed to be the same. In addition, the two crystallographic distinct Fe ions were also tightened to be the same. After the above setting, all parameters were

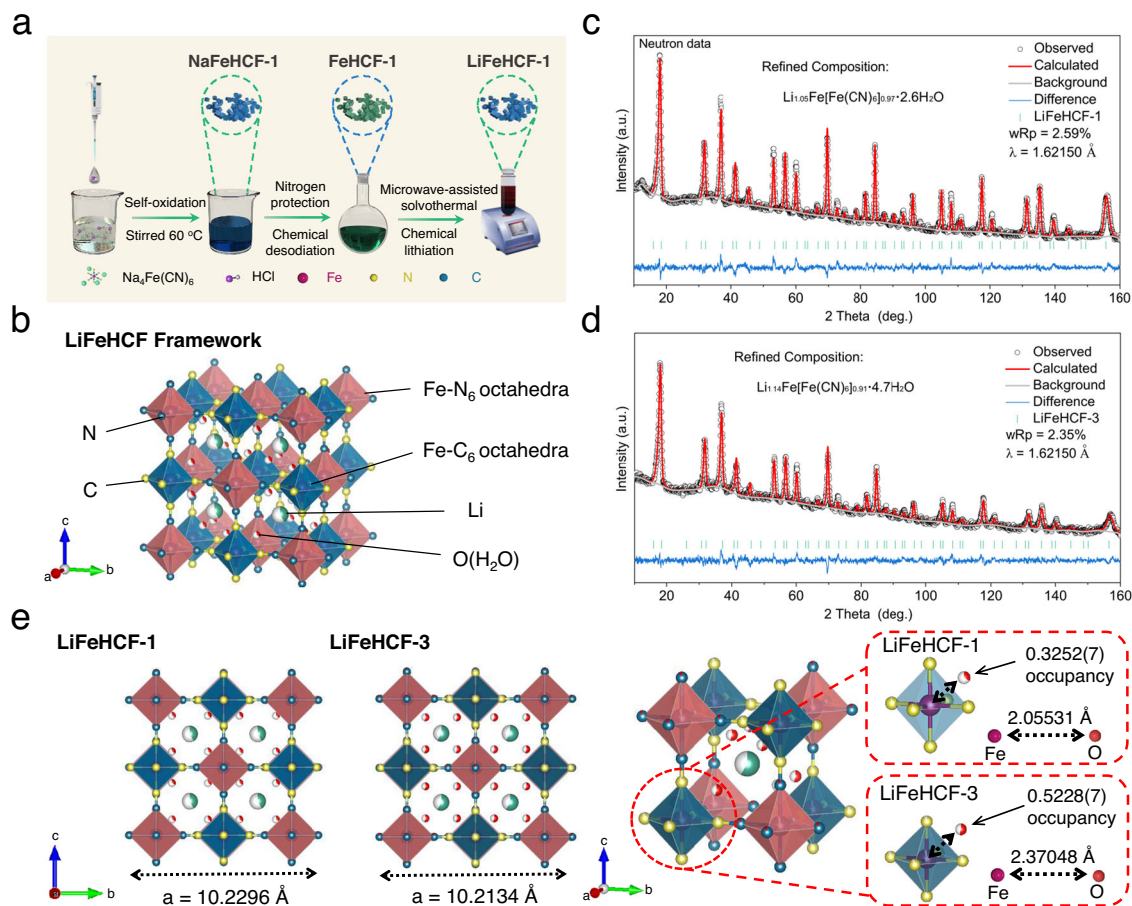


Fig. 1 | Material synthesis strategy and refinement results. **a** Schematic illustrations of the synthetic route for the LiFeHCF-1 sample. **b** Crystal structure of lithiated Prussian blue. Neutron diffraction patterns and Rietveld refinement results of the **c** LiFeHCF-1 and **d** LiFeHCF-3 samples. **e** Comparison of the unit cell

parameters and coordination environment between zeolitic water and $\text{Fe}(\text{CN})_6$ octahedra for the LiFeHCF-1 and LiFeHCF-3 samples. Lithium, carbon, nitrogen, iron (coordinated with carbon), iron (coordinated with nitrogen) and oxygen atoms are shown in green, blue, yellow, purple, dark blue and red colors, respectively.

allowed to change until Rietveld analysis went to convergent. This initial step was used to determine the $[\text{Fe}(\text{CN})_6]^{3-}$ vacancy concentration in the PBA structure.

Next, a Fourier-Transform neutron different map was conducted to find out the locations of coordinated and uncoordinated water molecules. It is also reported in the literature that Prussian Blue compounds comprise of various defects including $[\text{Fe}(\text{CN})_6]^{3-}$ vacancies and coordinated/uncoordinated water molecules, which could affect the structures. Based on the literature^{33,34}, H_2O molecules can be placed in the CN vacancy (Wyckoff site 24e). A local maximum was also found to be located at the Wyckoff site 32f (0.366, 0.366, 0.366) which is the part of the void in the structure. O ions were then added to the N defect locations (coordinated water) and the 32f sites (uncoordinated water) inside the unit cells. New constrains were created such that the O atoms were allowed to move between the above two sites while their total quantity was remaining constant. Once the Rietveld analysis was convergent, lithium ions position was determined by the Fourier-Transform neutron different map. Another local maximum was found to be located at the Wyckoff site 32f (0.25, 0.25, 0.25). Finally, lithium ions were added at the 32f sites in the unit cell. All of the Rietveld analysis can be convergent, and the agreement factor wRp (weighted R-factor profile) values were reasonably low (2.62%). All refinement results were summarized into Supplementary Tables 2–5. As shown in Fig. 1e, the LiFeHCF-1 sample demonstrates the lattice parameter increases from 10.2134 to 10.2296 Å as compared to LiFeHCF-3, which means higher diffusion coefficient for lithium ions³⁵. In addition, the higher occupancy of water and the longer Fe–O bond distance were

observed in LiFeHCF-3 samples. The water molecules located in vacancy can impede Li-ion migration, but suitable water closed to $\text{Fe}(\text{CN})_6$ octahedra may help maintain structure and avert the severe Li displacement in the $\langle 111 \rangle$ direction.

Electron paramagnetic resonance (EPR) is an effective characterization technique that can be used to verify the iron species in substances, especially when studying the coordination environment and oxidation state of transition metals³⁶. Figure 2a and Supplementary Fig. 8a illustrate that the EPR spectra of LiFeHCF-1, LiFeHCF-2 and LiFeHCF-3 samples have characteristic peaks at *g*-factor = 4.3 and *g*-factor = 2.03, respectively. The peak at *g*-factor = 4.3 is assigned to the four-coordinated or distorted four-coordinated isolated Fe^{3+} , while the peak with *g*-factor = 2.03 was assigned to the highly symmetrical six-coordinated isolated Fe^{3+} or the characteristic peak of polymeric iron ions^{37,38}. Different LiFeHCF samples show distinct coordination environment of iron bound to Fe–C₆ octahedra or FeN₆ octahedra. LiFeHCF-1 has a narrow peak at *g*-factor = 4.3, which is indicative of that highly symmetrical six-coordinated ferric iron ions and hence the high crystallinity and low defects. In contrast, LiFeHCF-2 and LiFeHCF-3 have relatively broad peaks at *g*-factor = 4.3, which suggests presence of the polymerized Fe ion with increased defects in lattice. The fragmented $\text{Fe}(\text{CN})_6$ group hinders Li-ion migration in the crystal structure.

The Fourier transform infrared spectroscopy (FTIR) and Raman spectroscopy (Raman) were also utilized to study the structural variation of LiFeHCF samples. Supplementary Fig. 8b shows the FTIR spectra of different LiFeHCF materials in the range of 500–4000 cm^{-1} . The characteristic peaks at 494 cm^{-1} and 608 cm^{-1} are assigned to the

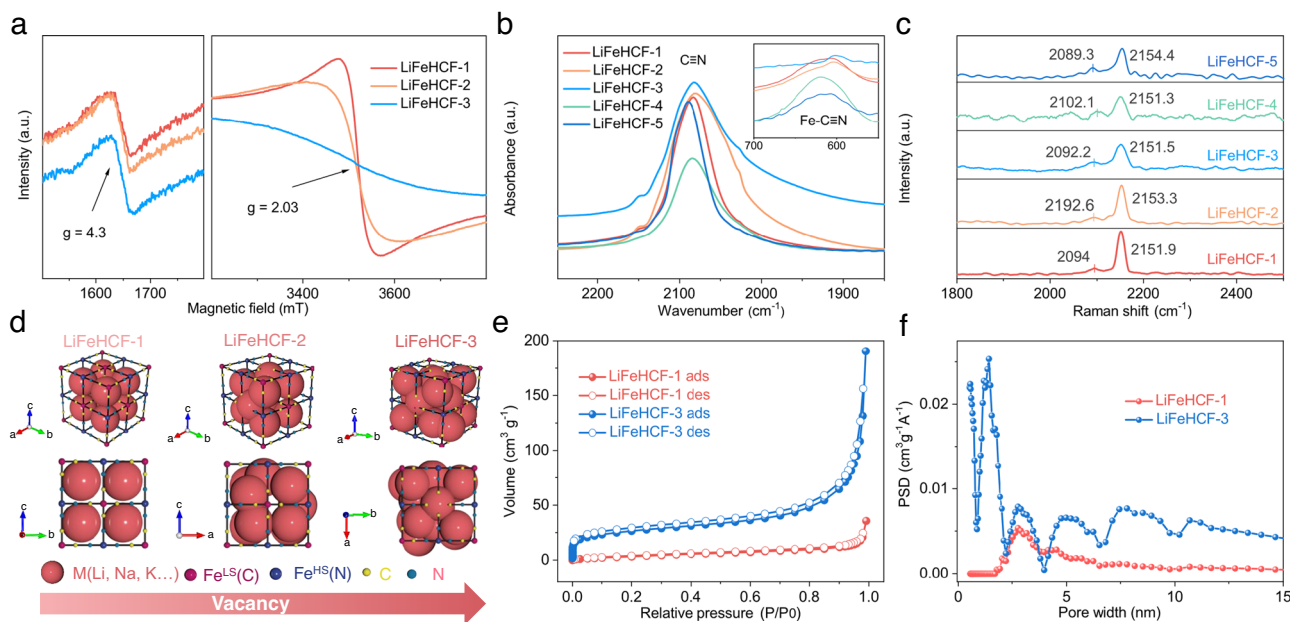


Fig. 2 | Structural characterization of different LiFeHCF samples. **a** Electron paramagnetic resonance (EPR) spectra of the LiFeHCF-1, 2, and 3 samples. **b** FTIR spectra of various LiFeHCF materials. The inset shows the enlarged plots of the spectra between 550 and 700 cm^{-1} . **c** Raman spectra (1800–2550 cm^{-1}) of LiFeHCF

showing the evolutions of the $(\text{C}\equiv\text{N})^-$ group. **d** Schematic illustrations of the characteristics of LiFeHCF samples and vacancy correlations. N_2 adsorption–desorption isotherms (**e**) and Pore-size distribution (**f**) of the LiFeHCF-1, LiFeHCF-3 samples.

out-of-plane bending vibration peak and the in-plane bending vibration peak of the Fe–C chemical bonds in the Fe–C≡N group, respectively^{39–41}. In addition, the peaks at 1638 cm^{-1} and 3462 cm^{-1} are O–H bond stretching vibration peaks and in-plane bending vibration peaks, and the peaks at 2082 cm^{-1} represents the stretching vibration peak of the C≡N bond that is related to the transition metal ions bonded to the CN⁻ groups. Notably, the stretching vibration peak of the C≡N bond, as shown in Fig. 2b, reveals the vibrations of Fe–C≡N group of LiFeHCF samples. Compared to LiFeHCF-3, LiFeHCF-1 has a blue shift and higher peak of Fe–C≡N at 608 cm^{-1} , which is attributed to the stronger C≡N chemical bond and more stable Fe–C≡N group. In Fig. 2c, Raman spectra (1800–2550 cm^{-1}) show the characteristic diffraction peak attributed to the C≡N groups bonded to iron ions of different valences in the lattice^{21,42}. The gradual increase of peaks at 2151 cm^{-1} and 2094 cm^{-1} indicates that the increased symmetry of the FeC₆ and FeN₆ octahedra, which is consistent with the EPR result. Based on the above analyses, Fig. 2d schematically illustrates the distribution of the Fe–C≡N group in LiFeHCF-1, LiFeHCF-2, and LiFeHCF-3. LiFeHCF-1 has more symmetric FeC₆ or FeN₆ octahedra, good crystallinity and lower defects among all samples, whereas the massively incomplete Fe–C≡N group in LiFeHCF-2 and LiFeHCF-3 possibly cause irreversible insertion/extraction of lithium ions and the increased space for zeolitic water. The different structures of LiFeHCF samples were further verified with the Nitrogen adsorption/desorption measurements and analyses. As shown in Fig. 2e, f, LiFeHCF-3 shows higher specific surface area (55 $\text{m}^2 \text{g}^{-1}$ vs. 15 $\text{m}^2 \text{g}^{-1}$) as well as more micropores (<2 nm) than for LiFeHCF-1. The high surface area is partially due to the reduced particle size of LiFeHCF-3 (see Supplementary Fig. 9), but also an indication of abundant defects resulted from the synthetic process. The Nitrogen adsorption/desorption measurements and analyses of LiFeHCF-2, LiFeHCF-4, and LiFeHCF-5 samples were also presented for comparison (Supplementary Fig. 10).

To further probe the local environment, X-ray photoelectron spectroscopy (XPS) measurements was performed with LiFeHCF samples (Supplementary Fig. 11). For high-resolution XPS spectra, the Fe 2*p* peaks are located at the binding energy of 724.7 eV and 709.8 eV, corresponding to Fe³⁺ 2*p*_{3/2} and Fe³⁺ 2*p*_{1/2}, respectively^{43,44}. Within the

binding energy regions of 721.2 eV and 708.4 eV, all LiFeHCF spectra show the characteristic peaks of Fe²⁺, but the signals of Fe³⁺ ions are not different from each other. The LiFeHCF-3 and LiFeHCF-5 samples have a bulging at -712 eV caused by polymeric iron ions, which is consistent with the ERP results.

It's generally recognized that water content has significant influence on electrochemical performance for Prussian cathodes^{10,32}. For this reason, thermogravimetric analysis (TGA) was performed to determine the presence and content of water in the lattice of LiFeHCF samples. In Supplementary Fig. 5, distinct weight loss between below 300 °C is attributed to the release of the adsorbed water and the coordinated water. The results were summarized in Fig. 3a revealing the mass loss of each LiFeHCF sample as 98.1%, 95.2%, 89.7%, 94.9%, and 81.8% at 150 °C, respectively. When the temperature was increased to 300 °C, the values were turned to 80.1%, 73.8%, 70.3%, 80.5%, and 68.6%, respectively. These results indicate less coordinated water in LiFeHCF-1 and LiFeHCF-4 samples. The more symmetric FeC₆ or FeN₆ octahedra in these samples lead to a decrease of water in lattice and the more stable structure; In contrast, the gradual increased defects in LiFeHCF-2, LiFeHCF-3, and LiFeHCF-5 samples lead to thermal instability, which is consistent with the previous conclusions.

The dehydration process and chemical degradation process of LiFeHCF samples were further studied with operando variable temperature XRD performed from 25 to 450 °C (Supplementary Fig. 12). Supplementary Fig. 13 is the schematic illustration of the stage with LiFeHCF powder in the heating module. Figure 3b, c (Supplementary Figs. 14 and 15) displays the TGA (DTA, differential thermal analysis) curves and the contour plots of the (200) and (220) diffraction peak of LiFeHCF-1 and LiFeHCF-3. The heating and the decomposition process can be sketched into three stages. In the first stage (stage a, from 25 °C to 100 °C), the (200) peak gradually shifts to higher angles and the (220) peak becomes weak, corresponding to the extraction of zeolitic water (adsorbed water) from lattice. Then the remaining zeolitic water (adsorbed water) continuously evaporate from defect sites, and the (200) and (220) peaks remain shifting and weakening from 100 °C to 250 °C/290 °C. When the temperature is increased to 300 °C/330 °C (stage b), the coordination water is deeply extracted from lattice and

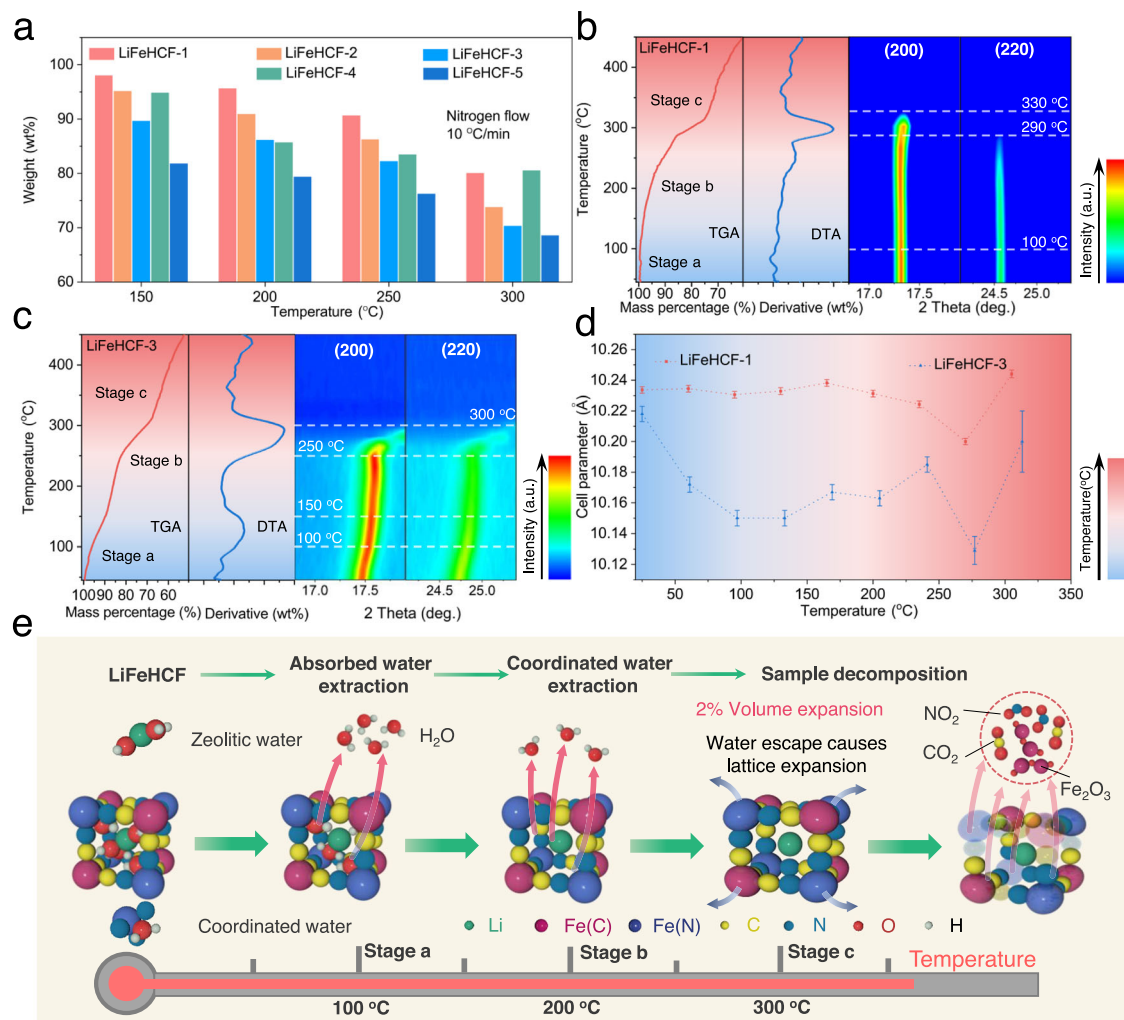


Fig. 3 | Characterizations of different LiFeHCF samples during the heating process. **a** The variation of weight in different LiFeHCF samples. Structural evolution of **b** LiFeHCF-1 and **c** LiFeHCF-3 powder samples during heating from 25 °C to 450 °C. **d** Comparison of the cell parameters changes of distorted framework of

LiFeHCF samples during heating process. The error bars represent the range of cell parameters for the Prussian blue samples upon heat treatment. **e** Schematic illustration of the dehydration behavior and the chemical degradation mechanism of LiFeHCF samples.

the samples evolve into an anhydrous phase. The disappearance of (200) and (220) peaks occurred at the 300 °C/330 °C due to the structural decomposition. We further applied the combined Thermogravimetry-infrared spectrometry (TGA-IR) technology for the LiFeHCF sample under flowing Ar protection (Supplementary Fig. 16), confirming the decomposition products include CO₂, NO₂ and HCN^{45,46}. Significantly, the LiFeHCF-3 sample exhibits relatively broadened and weakened diffraction peaks at stage a, indicating more zeolitic water was removed from the crystal lattice, resulting in severe lattice distortion and volume reduction. Figure 3d shows more detailed comparison of the cell parameter variation during heating. Due to the release of zeolitic water and coordination water, the cell parameter is decreased from 10.218 Å to 10.129 Å for LiFeHCF-3, and the unit cell volume is contracted by 2.7%. In comparison, LiFeHCF-1 has a little shrinking of 0.9% as the cell parameters is stable from 25 °C to 290 °C (10.201 Å vs. 10.23368 Å). Afterwards, the two LiFeHCF samples exhibit the lattice expansion with volume change of -1.2% and -2.1% until the samples start to decompose.

Collectively, the dehydration behavior and the chemical degradation process of LiFeHCF samples is summarized in the schematic illustration of Fig. 3e. Different types of water correspond to various extraction temperatures and lattice changes. The results also suggest that the presence of zeolitic water in the crystal lattice has negative

effects on thermal stability, which was in fact dominated by the increase of asymmetric Fe-C₆/Fe-N₆ octahedra. The correlations between thermal stability and zeolitic water content and the integrity of structural framework of LiFeHCF materials are not usually reported and discussed in the literature. The operando variable temperature XRD patterns of LiFeHCF-2 and LiFeHCF-4 show similar results as the LiFeHCF-1 and LiFeHCF-3 samples in Supplementary Figs. 17–20.

The scanning electron microscope (SEM) images for LiFeHCF-1, LiFeHCF-2, LiFeHCF-3, LiFeHCF-4 and LiFeHCF-5 powder samples are shown in Supplementary Fig. 9. LiFeHCF samples prepared by different methods possess similar cubic morphologies but different particles sizes (from nanometer to micrometer). In Supplementary Fig. 9a, d, the cubic features with smooth interface of LiFeHCF-1 and LiFeHCF-4 samples can be attributed to the self-decomposition synthesis methods with intrinsic slow nucleation rate (using Na₄Fe(CN)₆, Li₄Fe(CN)₆ as sodium source and lithium source, respectively). In contrast, LiFeHCF-2 and LiFeHCF-3 exhibit different morphologies with agglomerations from the other two samples, relating to the randomly aggregated process by the modified citrate-assisted co-precipitation method. Figure 4a–f shows the typical crystallite sizes of LiFeHCF samples. LiFeHCF-1 has largest size of ~4 μm and LiFeHCF-4 cube are only ~650–850 nm. LiFeHCF-1 sample possess a single-crystal morphology with high crystallinity, while LiFeHCF-2 and LiFeHCF-3

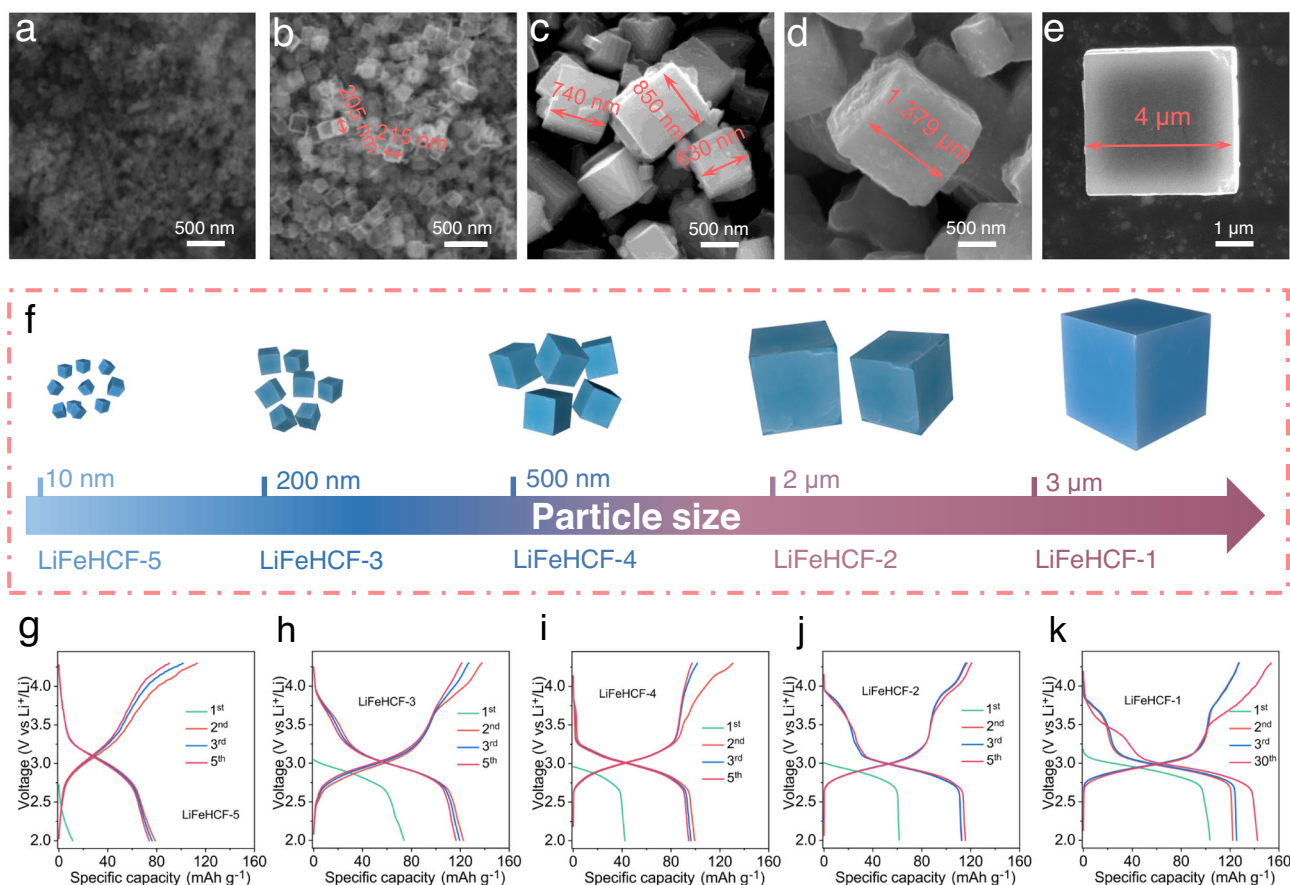


Fig. 4 | Influence of particle size on electrochemical performance of LiFeHCF samples. Particle size of **a** LiFeHCF-5, **b** LiFeHCF-3, **c** LiFeHCF-4, **d** LiFeHCF-2, and **e** LiFeHCF-1 powder samples. All images are taken from ex situ SEM measurements. **f** Schematic illustration of a microcrystalline crystallite size of LiFeHCF sample.

g–k The corresponding capacity–voltage profiles of the LiFeHCF samples at specific current of 19 mA g^{-1} . All LiFeHCF electrodes were evaluated in coin cell configuration using Li metal as counter electrode and tested at 25°C .

samples has the average crystallite sizes of $\sim 2 \mu\text{m}$ and $\sim 200 \text{ nm}$. Their precursors were synthesized by same coprecipitation method expect for using different content of sodium citrate. LiFeHCF-5 sample prepared by simple coprecipitation method (using $\text{Li}_4\text{Fe}(\text{CN})_6$) has the smallest size of $\sim 10 \text{ nm}$. All samples have different nucleation rates, and the fast crystallization may result in the presence of vacancies and the large content of zeolitic water, hindering the growth of crystallite sizes. We also attempted to directly observe the location of defects and water in the lithium-based Prussian blue lattice, but the samples too sensitive for high-resolution electron microscopy and spectroscopy, for this reason, PBA high-resolution images have rarely been reported⁴⁷.

Electrochemical performances of LiFeHCF samples

LiFeHCF electrodes were evaluated in coin cell configuration using Li metal as counter electrode with 1 M LiPF_6 in ethylene carbonate (EC) and diethyl carbonate (DEC) electrolyte. Figure 4g–k shows the Galvanostatic cycling curves of LiFeHCF-1, LiFeHCF-2, LiFeHCF-3, LiFeHCF-4 and LiFeHCF-5 samples at a specific current of 19 mA g^{-1} . The cells deliver discharge capacity of 126 mAh g^{-1} , 117 mAh g^{-1} , 122 mAh g^{-1} , 103 mAh g^{-1} and 80 mAh g^{-1} in the second cycle, respectively. It is worth noting that the LiFeHCF-1 sample with the largest particle size has an activation process and the highest discharge capacity of 143 mAh g^{-1} appears after 30 cycles (Fig. 4k). Supplementary Fig. 21a give a comparison between crystallite size and electrochemical energy storage performance of LiFeHCF samples. It has been demonstrated that the crystallite size is closely related to the electrochemical behaviors of potassium Prussian white materials ($\text{K}_{1.7}\text{Fe}[\text{Fe}(\text{CN})_6]_{0.9}$)⁴⁸. The K-based

Prussian blue sample with a small size ($\sim 20 \text{ nm}$) shows the best electrochemical performance; however, the micron-sized Prussian blue samples seem more suitable for lithium-ion batteries.

The typical discharge voltage plateau at 3.1 V can be observed for all samples, but the LiFeHCF-1, LiFeHCF-2 also have a second plateau at 3.8 V , which correlate with the reduction reactions $\text{Fe}^{3+}/\text{Fe}^{2+}$ couples during the lithiation process. Cyclic voltammetry (CV) test was performed to understand the reasons for various voltage plateau of LiFeHCF samples. As shown in Fig. 5a, the cathodic peaks at 3.1 V belongs to the redox reactions of high-spin $\text{Fe}^{3+}/\text{Fe}^{2+}$ couples coordinated with nitrogen, and the high-potential peaks at 3.8 V are related to the low-spin $\text{Fe}^{3+}/\text{Fe}^{2+}$ couples coordinated with carbon⁴⁹. The CV curves of other LiFeHCF samples under the same test conditions are shown in Supplementary Fig. 21b–d. The peaks do not appear in high voltage range for LiFeHCF-3, indicating there is correlation between Fe-C_6 octahedra and redox potentials upon lithium ions insertion/extraction.

Rate capability of LiFeHCF electrodes were furthered investigated in non-aqueous Li metal coin cell configuration as shown in Fig. 5b and Supplementary Fig. 22. Li metal cells with LiFeHCF-1-based positive electrodes show the best performance among all samples. The capacities are $135, 131, 128, 122, 107,$ and 97 mAh g^{-1} at $38, 95, 190, 380, 950,$ and 1900 mA g^{-1} , respectively. Also, the LiFeHCF-1 electrode demonstrates superior cycling performance at 190 mA g^{-1} , delivering a reversible capacity of 109 mAh g^{-1} and good retention of $\sim 90\%$ after 650 cycles. In comparison, the capacities of LiFeHCF-2, LiFeHCF-3, LiFeHCF-4, and LiFeHCF-5 electrodes at 190 mA g^{-1} are $87, 41, 61, 29 \text{ mAh g}^{-1}$ and capacity retention of $82.3\%, 40\%, 70\%,$ and 47.4% , respectively (Fig. 5c). Significant capacity fading occurs after 100

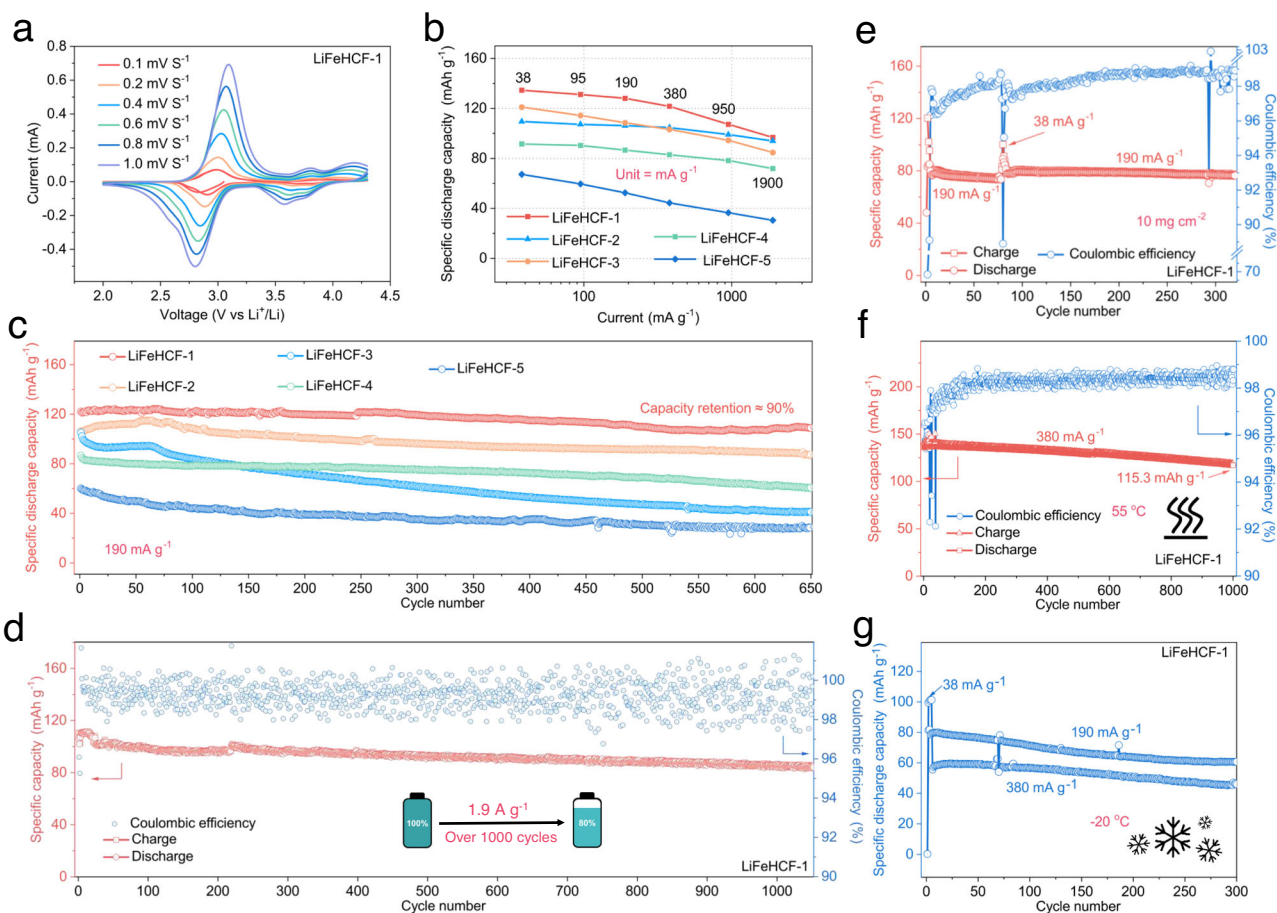


Fig. 5 | Electrochemical evaluation of LiFeHCF-1 samples. **a** Cyclic voltammetry curves of LiFeHCF-1 sample at different scanning rates. **b** Rate performance of LiFeHCF samples at various specific currents. **c** Cycling performance of LiFeHCF samples at 190 mA g⁻¹. **d** Long-term cycling of LiFeHCF-1 material at 1.9 A g⁻¹. **e** High-loading performance (10 mg cm⁻²). **f, g** High and low temperature tests at 55 °C and

-20 °C. All LiFeHCF electrodes were evaluated in coin cell configuration using Li metal as counter electrode and tested at 25 °C (except where differently indicated). The specific capacity values were calculated based on the mass of positive electrode active material.

cycles for LiFeHCF-3 and LiFeHCF-5. The poor stability is possibly related to the large number of vacancies that hinder Li-ion migration through the <100> direction. Besides, the zeolitic water in the structures is gradually extracted during the charge/discharge process, further accelerating electrolyte decomposition and reducing coulombic efficiency. The LiFeHCF-1 electrode exhibits noticeable long-term cycling performance at a high specific current of ~1.9 A g⁻¹. As shown in Fig. 5d, the cell delivers a discharge capacity of 118.9 mAh g⁻¹ at the initial cycle and maintains 80.7% capacity over 1000 cycles (0.019% capacity fading per cycle) with a high coulombic efficiency of 99.3%. Even positive electrodes with a mass loading of 10 mg cm⁻², the Li metal coin cell has a capacity retention of 98% after 300 cycles at 190 mA g⁻¹ (Fig. 5e); it also shows good performance at 55 °C and -20 °C (Fig. 5f and g). Supplementary Table 6 summarizes the electrochemical performances of representative Na-PBA cathodes and our LiFeHCF, highlighting its potentials for the application in LIBs.

To better evaluate the relation between discharge and lithium-ion diffusion properties, galvanostatic intermittent titration technique (GITT) measurement was performed by inserting Li⁺ into LiFeHCF samples at a specific current of 190 mA g⁻¹ between 2.0 and 4.3 V, and the cell was discharged from 4.3 V for 10 min followed by a rest of 120 min. As shown in Supplementary Fig. 23, the sloping regions at 3.8–3.5 V and 2.7–2.0 V are indicative of solid solution process, while the overpotential between 3.2–2.7 V (corresponding to lithium insertion from Li_{0.5}FeFe(CN)₆ to Li_{1.8}FeFe(CN)₆) and the flat sloping region indicates two-phase mechanism of the insertion of more lithium^{49,50}.

Investigation of phase transitions of LiFeHCF-1 sample during cycling

Operando XRD was conducted to study the phase transitions during Li⁺ insertion and extraction in the LiFeHCF-1 sample. The digital image and schematic illustrations of the operando XRD cell and instrument are shown in Supplementary Fig. 24a, b. In Fig. 6a, the peaks at 17.8° and 35.5° are gradually shifted to lower angles and the peak at 25° is disappeared (Supplementary Fig. 24c), indicating the increases of the volume of the unit cell on lithiation. The peaks are recovered at the initial position after 2nd discharge, suggesting the formation of Li-rich Li_{1+x}FeFe(CN)₆. It is worth mentioning that this phenomenon is different from the observation of irreversible lattice shrinking with Na Prussian blue materials⁵⁰. The cubic unit cell and the ease of movement of lithium ions for LiFeHCF-1 material have a highly reversible phase transition that helps long cycle life (over 1000 cycles at 1.9 A g⁻¹).

The expanded views of the (200), (220), and (400) peak regions are shown in Fig. 6b. The (200) peak gradually shifts from 17.8° to 17.52° upon the first discharge process, which indicates the evolution of the cell parameters during the second lithium intercalation process. The full insertion of Li⁺ to Li_{1+x}FeFe(CN)₆ lattice evolved a new phase when the voltage reached 2.0 V. The subsequent charge shows the recovery of peak, corresponding to the deintercalation of Li⁺ vs. Li_{2-x}FeFe(CN)₆ and FeFe(CN)₆. Notably, the (200) and (400) diffraction peaks are recovered after re-discharged to 2.0 V, confirming the high reversibility of the Li_{2-x}FeFe(CN)₆ phase during Li intercalation/deintercalation. This highly reversible Li migration process is likely to

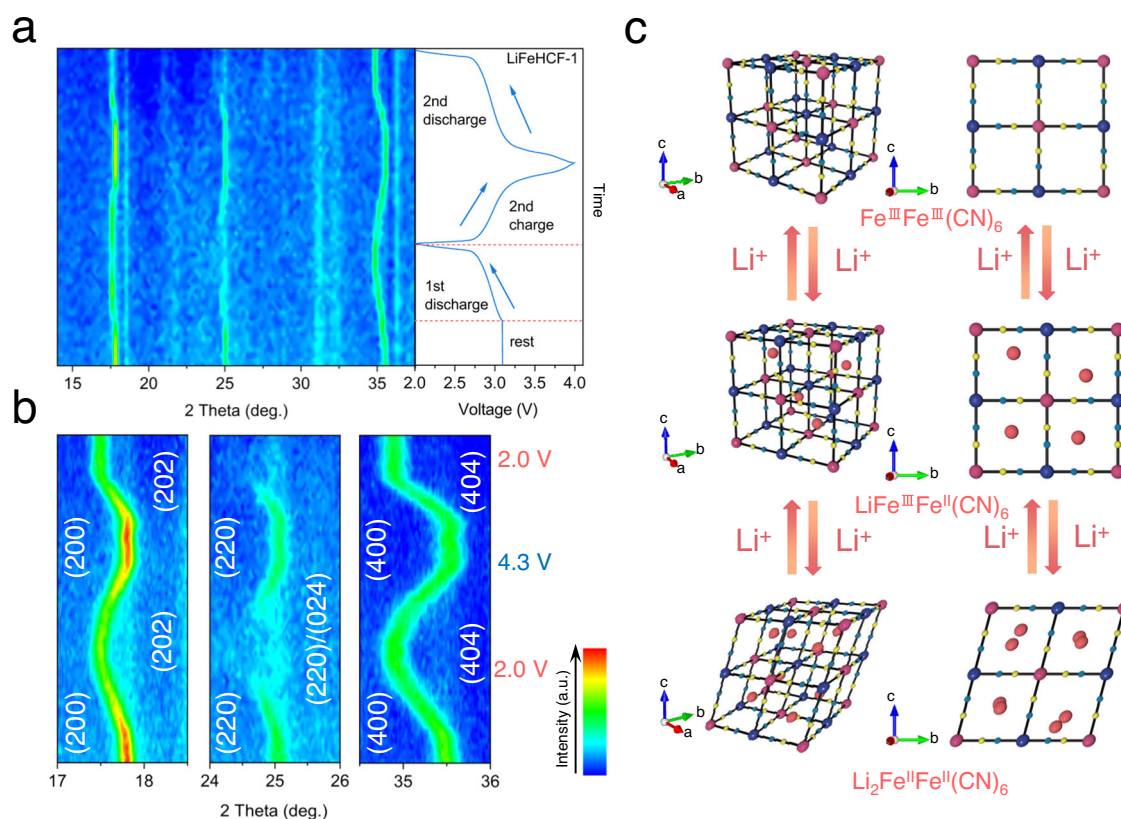


Fig. 6 | Structural evolution of the LiFeHCF-1 sample during charge and discharge. **a** Operando XRD patterns. **b** Detailed information of the (200), (220)/(024), and (400) diffractions. **c** Schematic of the phase evolutions upon Li

insertion/extraction. The Operando battery for XRD testing was carried out by stainless steel cell with beryllium window at specific current of 9.5 mA g^{-1} at 25°C .

be attributed to the more symmetric Fe–C₆/Fe–N₆ octahedra of the LiFeHCF-1 sample. Also, the (220) diffraction at 25° splits into two peaks after discharged to 2.0 V, which is another evidence of high lithiation degree of the LiFeHCF-1-containing positive electrode. As schematically illustrated in Fig. 6c, it is assumed that the onset of Li diffusion is through the $\langle 100 \rangle$ direction for the cubic Fe^{III}Fe^{III}(CN)₆. Upon the subcube sites are half-occupied, the diffusion path is changed to the $\langle 111 \rangle$ direction due to the volume expansion accompanied by the lattice transformation from cubic LiFe^{III}Fe^{III}(CN)₆ to rhombohedral structure Li₂Fe^{II}Fe^{II}(CN)₆, which is in agreement with the GITT results.

Lithium-ion and water molecules diffusion behavior

To understand the Li-ion diffusion behaviors, bond valence energy landscape (BVEL) calculations was performed with LiFeHCFs. Since the C and N atoms are covalently bonded together in the CN ligands, the correct charge on C and N could not be easily determined. Nonetheless, we arbitrarily assigned C and N with three different scenarios: 1. C4+ and N3–, and 2. C3+ and N3–, and 3. C4+ and N3–. We expect that the exact energy barrier would be estimated with uncertainty. However, such a method could still be useful to illustrate the topology of the pathways of lithium ions. As shown in Fig. 7a, we reveal that Li-ion diffusion can proceed through the a $3.2 \times 2.0 \text{ \AA}^2$ ellipsoid pore window centered at (0.25, 0.25, 0) into the 3D-interconnected cubic $3 \times 3 \times 3 \text{ \AA}^3$ nano-cage centered at (0.25, 0.25, 0.25). The diffusion of lithium ions was mainly driven by two factors: 1. the columbic interaction between the negative charged framework and the position of the charge on the lithium ions when the Fe ions were undergone reduction reaction to change their valence states from 3+ into 2+, upon the discharging process; 2. the chemical potential different between the PBA compounds and its surrounding environment.

In Supplementary Fig. 25, since the occupancy of H₂O molecules is 0.32 at the 32f site (0.25, 0.25, 0.25) in the unit cell, the probability to H₂O molecule at this site was 32%. The topological pathway was very similar to the simulation without putting an addition water molecule in the unit cell (Supplementary Figs. 26, 27 and Table 7). However, the density of the percolation network was found to shrink significantly, as we compared the same bond valence mismatch value of 1. This indicated that the water molecule can reduce very significantly on the conductivity of the lithium ions in the unit cell. If the water content is increased in the framework, the apparent percolation network will shrink significantly. Therefore, the lithium-ion conductivity will be dropped dramatically.

Recently, a few computational studies have tried to explain how water molecules can stabilized the structure of PBAs upon electrochemical cycling^{51,52}. This enlighten us to further investigate diffusion behaviors of water molecules in PBAs as water molecules could be exchanged between the non-aqueous electrolyte solution and the PBA structure during the charge/discharge processes. As shown in Fig. 7b, c, the BVS mismatch map on PBA indicates the diffusion pathway of water molecules are resemble but wider spread behavior as the Li-ion percolation network. This suggests that water molecules could easily block the diffusion pathway of Li-ions if their concentration is high (>1.8 mol% or 9.8 wt.%). Therefore, minimizing the water content and the defects in PBAs could help to optimize the electrochemical energy storage performances of Li-based cells with PBAs-containing positive electrodes.

As shown in Supplementary Fig. 28, additional supercell analysis was performed to enlarge the unit cells along x by 2 and along y by 2 to provide better understanding on the effect of H₂O molecules in space as they can either occupy or un-occupy into the 32f sites. Of 32 sites in the supercells, 10 of them will be filled with H₂O molecules. This will

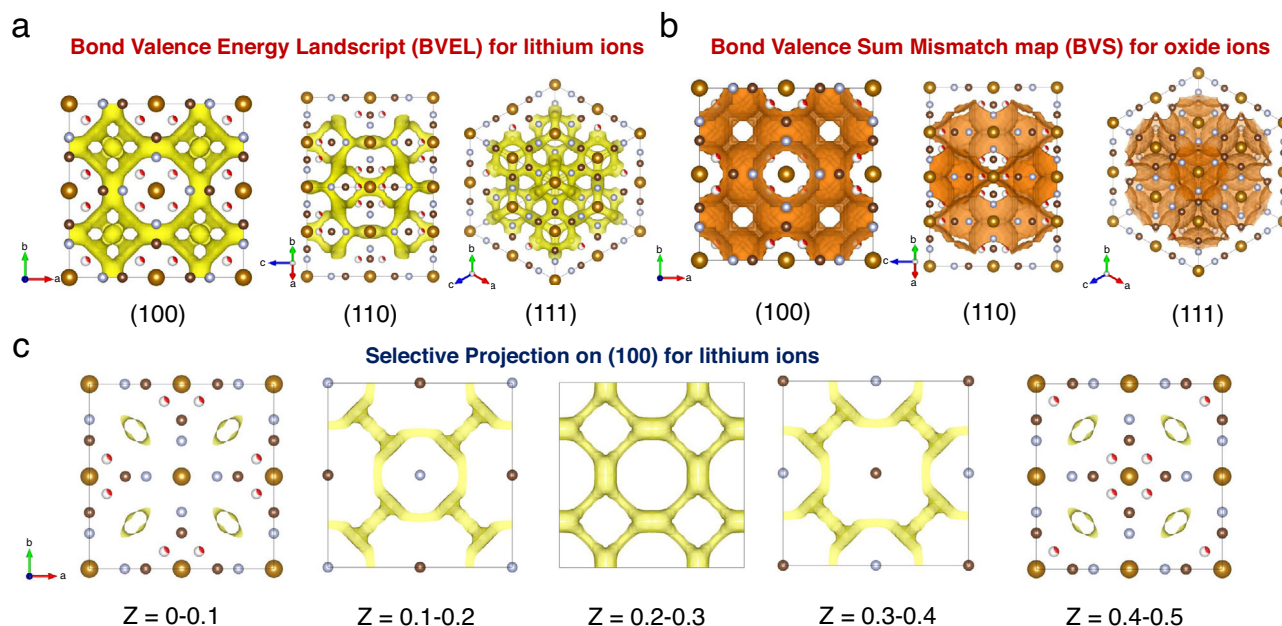


Fig. 7 | Theoretical prediction of the pathways of Li-ions for PBAs. **a** Bond Valence Energy Landscape (BVEL) calculation for Li-ions in LiFeHCF samples. **b** Bond Valence Sum Mismatch map (BVS) calculation for oxide ions in LiFeHCF

samples. The selected projection on (100), (110) and (111) planes were presented, indicating that Li-ions can be transported 3-dimensionally through the void of PBA compounds. **c** BVEL with different Z values on the (100) planes.

come with a total combination of 64512240. Thanks to the supercell program, the coulombic energies of all supercells can be calculated and ranked based on their energies for outputting. Below is the additional BVEL analysis on the lowest energy supercell to show the effect of H₂O on the lithium-ion diffusion property. First, it is interesting that water molecules are not evenly distributed inside the supercell, while some of them like to aggregate to form water clusters. With a small value of BVEL, 3D percolation network can be observed but they are formed around the water clusters. As we progressively increase the BVEL values, lithium ion diffusion network can also form as they pass through the void where water molecules are absent. Interestingly, the increase in the density of 3D percolation network is mainly due to the new pathways with void, while the original pathways, with water clusters nearby, is hardly changed. Therefore, we can conclude that an excess of water molecules will decrease the over density of lithium-ion percolation network in the structure.

Electrochemical performance of LiFeHCF-1-based positive electrodes in Li-ion coin cell configuration

To further validate the practical application of the LiFeHCF-1 cathode, Li-ion cells were assembled and tested with commercial graphite as the negative electrode active material (Fig. 8a and Supplementary Fig. 29). At a specific current of 38 mA g⁻¹ (considered the mass of positive electrode active material), the graphite||LiFeHCF-1 coin cell gave a reversible capacity of 106 mAh g⁻¹ (Fig. 8b) with an average discharge voltage around 2.9 V, no capacity attenuation was appeared after 5 cycles over the voltage range of 1.5 ~ 4.0 V. In Fig. 8c, d, the full cell showed good reversible capacity 104, 102, 99, 95 mAh g⁻¹ at different rates of 95 mA g⁻¹, 190 mA g⁻¹, 380 mA g⁻¹ and 950 mA g⁻¹, respectively, and the specific capacity could be recovered to 109 mAh g⁻¹ at specific current of 38 mA g⁻¹. Interestingly, the cell can be cycled up to 1.9 A g⁻¹ delivering a specific discharge capacity of about 90 mAh g⁻¹. Furthermore, Fig. 8e shows a high capacity of 105 mAh g⁻¹ and capacity retention of 98% (average coulombic efficiency ≈ 99.6%) over 370 cycles.

In summary, we systematically studied the preparation of various LiFeHCF samples and compared their Li-ion storage performance in a non-aqueous environment. The impacts of zeolitic and crystal water in terms of thermal stability and structural framework integrity have been

revealed by using advanced technologies including powder neutron diffraction, thermogravimetry-infrared spectrometry, operando variable temperature X-ray diffraction and Bond Valence Energy Landscape calculations. The tailored LiFeHCF material with micron size and single crystal morphology exhibits high capacity of >140 mAh g⁻¹ (at 19 mA g⁻¹) and long lifespan over 1000 cycles, as well as appealing performance under practical conditions such as high loading (10 mg cm⁻²), wide temperature (-20 to 55 °C) window and Li-ion cell configuration (graphite||LiFeHCF).

Methods

Materials synthesis

LiFeHCF-1, LiFeHCF-2 and LiFeHCF-3 were prepared by the ion-exchange method from NaFeHCFs^{53,54}. Typically NaFeFe(CN)₆-1 (NaFeHCF-1) was first obtained via self-oxidation/precipitation^{55,56}. First, 2 mmol sodium ferrocyanide (Na₄Fe(CN)₆, 99.7%, Aladdin) were dissolved in 100 ml deionized water to afford clear solution under stirring (400 rpm). Next, 1 mL of hydrochloric acid (37 wt% solution in water, Acros) was added dropwise to the solution, and then the solution was heated at 60 °C under vigorous stirring (600 rpm) for 4 h. The resulting dark blue suspension was collected by centrifugation (8000 rpm, 5 min), washed with water (40 ml) and ethanol (40 ml) three times, and dried in vacuum oven at 100 °C for 24 h to obtain NaFeHCF-1. FeFe(CN)₆-1 (FeHCF-1) was prepared by chemical desodiation using tetrafluoroborate (NO₂BF₄, 96%, Alfa, excess 50%) under nitrogen atmosphere with ultra-dry acetonitrile medium (99.9%, water ≤ 30 ppm, Innochem). LiFeFe(CN)₆-1 (LiFeHCF-1) was synthesized by chemical lithiation through a microwave-assisted solvothermal (MW-ST) process (using Anton Paar Monowave 400, 600 rpm) at 80 °C. Lil (99.9% metals basis, Aladdin) was served as both lithium source and reducing agent. The obtained sample were collected by centrifugation (8000 rpm, 5 min), washed by acetonitrile anhydrous and vacuum-dried 12 h at 100 °C.

The LiFeHCF-2 and LiFeHCF-3 samples were prepared by the same route except for the different NaFeHCF-2 and NaFeHCF-3. Here both NaFeHCF samples were synthesized by a modified citrate-assisted coprecipitation method^{20,57}. Briefly, 6 mmol iron sulfate heptahydrate (FeSO₄·7H₂O, 99.5%, Acros) and 25 g (NaFeHCF-2) or 5 g (NaFeHCF-3) of sodium citrate (C₆H₅Na₃O₇, 98%, Aladdin) were dissolved in 100 mL of

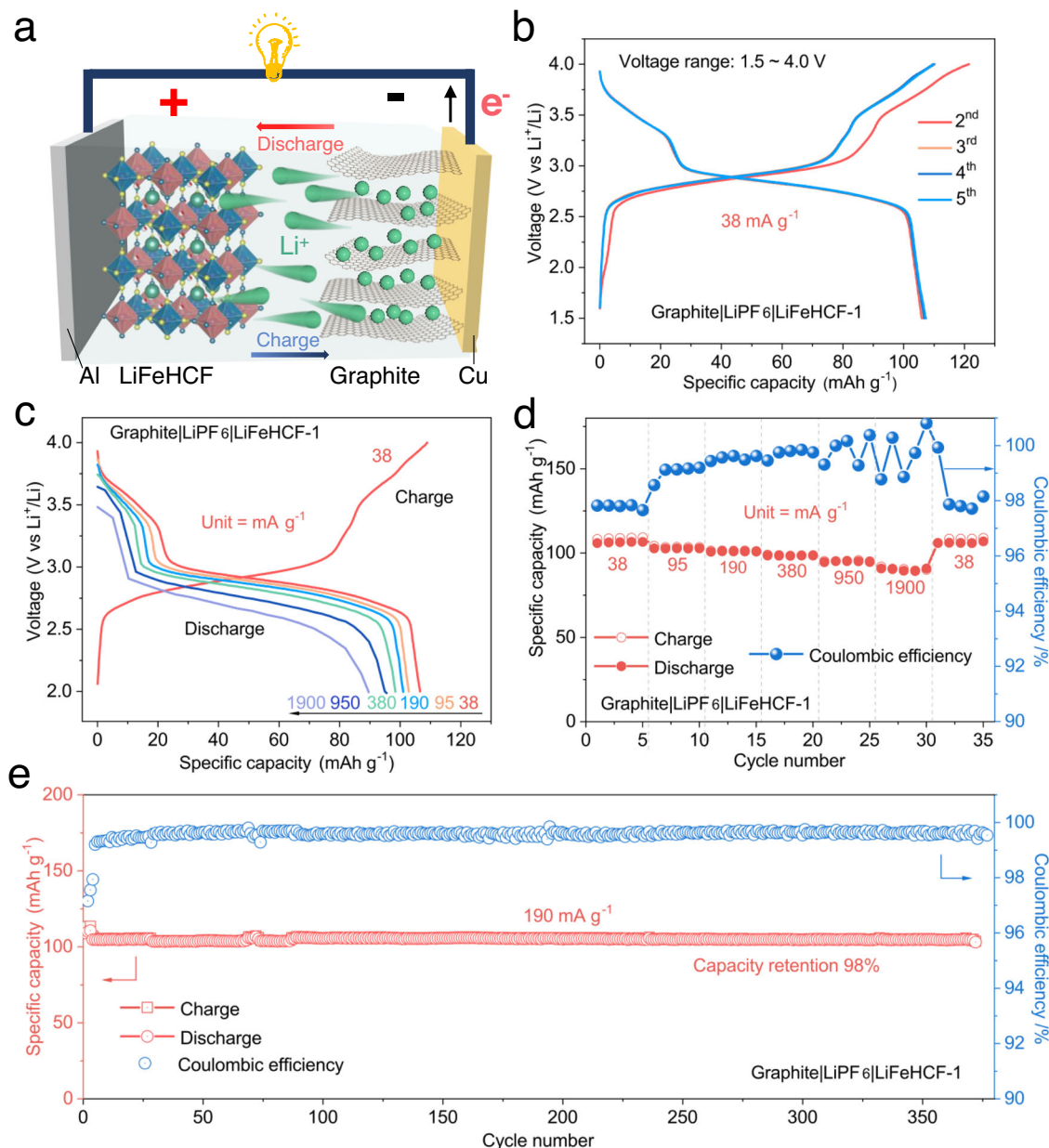


Fig. 8 | Electrochemical performance of LiFeHCF-1-based positive electrodes coupled with graphite-based negative electrodes. **a** The schematic illustration of the graphite ||LiFeHCF full cell. **b** Galvanostatic charge-discharge voltage profiles of the full-cell at 38 mA g⁻¹. Voltage profiles (c) and rate capability (d) at different

current densities from 38 mA g⁻¹ to 1900 mA g⁻¹. **e** The demonstration of long-term cycling of the cell at 190 mA g⁻¹. All LiFeHCF graphite||LiFeHCF full cell were tested at 25 °C and the specific capacity values were calculated based on the mass of positive electrode active material.

deionized water, stirring (400 rpm) until a clear solution A was formed. 4 mmol Na₄Fe(CN)₆ was added to 100 mL deionized water, labeled as solution B. Then, solution A was slowly added to solution B under vigorous stirring (600 rpm) and a milky white precipitate formed immediately. The mixture was stirred 12 h, and the product were collected by centrifugation (8000 rpm, 5 min), washed by deionized water (40 ml) and ethanol (40 ml) and vacuum-dried 24 h at 100 °C.

LiFeFe(CN)₆-4 and LiFeFe(CN)₆-5 (LiFeHCF-4 and LiFeHCF-5) samples were prepared using lithium ferrocyanide (Li₄Fe(CN)₆). Li₄Fe(CN)₆ samples was synthesized following the same methodology as reported in previous literature^{58,59}. Briefly, 56 mmol potassium ferrocyanide (K₄Fe(CN)₆, 99%, Acros) was dissolved in 25 ml deionized water, and 14 mmol lithium perchlorate (LiClO₄, 99.99%, Aladdin) solution were mixed with continuous magnetic stirring (400 rpm). A white precipitate of potassium perchlorate was formed, which was removed by centrifugation (8000 rpm, 3 min), while the solution was

heated to 70 °C to remove partial water. Next, the obtained solution was placed in a refrigerator overnight to allow potassium perchlorate was precipitated. The above steps were repeated several times until no KClO₄ precipitation was observed. The Li₄Fe(CN)₆ was dried at 150 °C. LiFeHCF-4 and LiFeHCF-5 was prepared by the same method as NaFeHCF-1 and NaFeHCF-3 except used Li₄Fe(CN)₆ without citrate used during the synthesis.

Materials characterizations

The obtained LiFeHCF samples were investigated by powder XRD analysis (Rigaku Miniflex 600) equipped using Cu Kα radiation at 40 kV and 20 mA. The crystal structure of LiFeHCF samples was analyzed by neutron diffraction. The diffraction data (LiFeHCF-1, 3 and 4 samples) was collected at the ECHIDNA high-resolution powder diffractometer with a monochromatic wavelength of 1.6215 Å in Australian Nuclear Science and Technology Organization (ANSTO). TOF neutron

diffraction measurement of LiFeHCF-2 was conducted at Multiple Physics Instrument (MPI) in China Spallation Neutron Source (CSNS). 2–3 g of powders were put into vanadium cans and the measurement time was about 3 h for each sample. The diffraction data was subsequently analyzed by GSAS EXPGUI⁶⁰. The content of Li, Fe, C, N elements in the LiFeHCF samples were identified by ICP analysis (OPTIMA 8000DV Optical Emission Spectrometers) and Element analyzer (Vario EL Cube), the relative standard deviation of the measured samples was less than 1.5%. Scanning electron microscopy (SEM) images were performed by FEI Verios 460 L. X-ray photoelectron spectroscopy (XPS) was taken on an ESCALAB250Xi (Thermo Scientific) spectrometer equipped with X-ray source ($h\nu=1486.6$ eV, monochromatic Al K α , 150 W). Fourier transform infrared (FTIR) spectra were carried out on a Fourier transform infrared spectrometer (Perkin Elmer) with KBr disk method. Raman spectra were measured at a Raman microscope with a 325 nm excitation laser (HORIBA JOBIN YVON S.A.S.). Nitrogen adsorption/desorption measurements were performed on Autosorb-iQ-MP (Quantachrome), the micropore surface areas, pore size distribution and pore volumes were determined from nitrogen (N₂) adsorption branch at 77 K with Brunauer–Emmett–Teller (BET) theory and the Barrett–Joyner–Halenda (BJH) model. EPR spectra were recorded from Bruker EMXplus-6/1 EPR spectrometer (9065.8 MHz, X band, 300 K). Thermogravimetry coupled with infrared spectrometry (TGA-IR) techniques (Perkin Elmer, Frontier Mid-IR FTIR/STA6000-TL9000-Clarus SQ8) was employed to confirm the decomposition products. Operando variable temperature X-ray diffraction measurement was performed on Rigaku Miniflex 600 from 25 °C to 450 °C, the powders sample was placed in heating module (Supplementary Fig. 13).

Electrochemical measurements

The LiFeHCF electrodes slurry were coated from N-methyl-2-pyrrolidone (NMP, 99.9%, Aladdin) onto aluminum collectors using polyvinylidene fluoride (PVDF, 99.9%, Arkema) as the binder. The typical electrode was made with a formula of active material (LiFeHCF powder): Super P (99.9%, Lion corporation): PVDF = 70:20:10. Then the electrodes were vacuum dried at 100 °C for 12 h and the active mass loading was -1.5 mg cm⁻². CR2032 lithium coin cells were fabricated inside an Ar-filled glovebox (H₂O < 0.1 ppm, O₂ < 0.1 ppm) with 1 M LiPF₆ in diethyl carbonate (DEC) and ethylene carbonate (EC) (1:1 vol/vol) electrolyte (water content < 10 ppm), a metallic lithium (0.45 mm, 99.9%, Innochem) negative electrode, and celgard separator (25 μ m, 55% porosity, 0.064 μ m pore size). The charge-discharge test was carried out on Land CT2001A battery cycler and tested in constant temperature test room (25 \pm 1 °C, except where differently indicated). The high and low-temperature tests were investigated on the high-low temperature test chamber (SHIPAC, operating temperature range: - 75 °C–150 °C \pm 1 °C). The specific capacity was obtained based on the mass of positive active material and at least two parallel cells were tested for individual electrochemical experiment. Cyclic voltammetry (CV) tests were conducted on an Ivium electrochemical Workshop between 2.0–4.3 V vs. Li/Li⁺ at various scan rates of 0.1 mV s⁻¹, 0.2 mV s⁻¹, 0.4 mV s⁻¹, 0.6 mV s⁻¹, 0.8 mV s⁻¹, and 1.0 mV s⁻¹. GITT testing of coin cell at 9.5 mA g⁻¹ between 2.0–4.3 V, in which the cell was discharged for 10 min followed by 120 min resting. The Operando XRD test was carried out with a stainless steel electrochemical cell with beryllium window at 9.5 mA g⁻¹ from 2.0 to 4.0 V, which was assembled with metallic lithium negative electrode, Celgard separator, and positive electrode. The full cell was assembled with commercial graphite (50–90 μ m, 99.7%, Shenzhen Kejing Star) as the anode, and the graphite electrodes were made by commercial graphite (90 wt%) and PVDF (10 wt%). The loading mass of LiFeHCF and graphite was -1.5 mg cm⁻² and the LiFeHCF/Graphite mass ratio is 1:0.8. The slurry in NMP was coated on copper foil (9 μ m, 99.8%, Shenzhen Kejing Star) and dried under vacuum at 120 °C.

Calculation method

The lithium-ion migration behavior was estimated by 3DBVSMAPPER. In particular, Bond Valence Energy Landscapist (BVEL) was calculated by lithium-ion migration pathways in two situations: 1. Valence states of C, N, O, and Fe were assigned as +2+, +3, -2 and +3; 2. Valence states of C, N, O and Fe were assigned as +4, +3, -2, and +3, respectively. The two calculated percolation networks were very similar with each other, indicating the deviation of valence state for C between 2 and 4 was not sensitive to the diffusion pathway. Similarly, the water diffusion pathway was also analyzed by the same methods. Two Valence states of C, N, O were separately considered as +4, +3, -2 and +2, +3, -2, respectively. The diffusion percolation networks were found to be non-sensitive with the valence states of C and N atoms.

Data availability

The data that support the findings of this study are available from the corresponding author upon reasonable request. Source data are provided with this paper.

References

1. Tarascon, J.-M. & Armand, M. Issues and challenges facing rechargeable lithium batteries. *Nature* **414**, 359–367 (2001).
2. Armand, M. & Tarascon, J.-M. Building better batteries. *Nature* **451**, 652–657 (2008).
3. Goodenough, J. B. & Kim, Y. Challenges for rechargeable Li batteries. *Chem. Mater.* **22**, 587–603 (2010).
4. Ohzuku, T., Ueda, A. & Nagayama, M. Electrochemistry and structural chemistry of LiNiO₂ (R3m) for 4 volt secondary lithium cells. *J. Electrochem. Soc.* **140**, 1862–1870 (1993).
5. Noh, H.-J., Youn, S., Yoon, C. S. & Sun, Y.-K. Comparison of the structural and electrochemical properties of layered Li[Ni_xCo_yMn_z]O₂ ($x = 1/3, 0.5, 0.6, 0.7, 0.8$ and 0.85) cathode material for lithium-ion batteries. *J. Power Sources* **233**, 121–130 (2013).
6. Chen, Z. & Dahn, J. R. Reducing carbon in LiFePO₄/C composite electrodes to maximize specific energy, volumetric Energy, and tap density. *J. Electrochem. Soc.* **149**, A1184 (2002).
7. Padhi, A. K., Nanjundaswamy, K. S. & Goodenough, J. B. Phospho-olivines as positive-electrode materials for rechargeable lithium batteries. *J. Electrochem. Soc.* **144**, 1188–1194 (1997).
8. Ryu, H.-H., Park, K.-J., Yoon, C. S. & Sun, Y.-K. Capacity fading of Ni-Rich Li[Ni_xCo_yMn_{1-x-y}]O₂ ($0.6 \leq x \leq 0.95$) cathodes for high-energy-density lithium-ion batteries: bulk or surface degradation? *Chem. Mater.* **30**, 1155–1163 (2018).
9. Zhou, A. et al. Hexacyanoferrate-type Prussian blue analogs: principles and advances toward high-performance sodium and potassium ion batteries. *Adv. Energy Mater.* **11**, 2000943 (2021).
10. Hurlbutt, K., Wheeler, S., Capone, I. & Pasta, M. Prussian blue analogs as battery materials. *Joule* **2**, 1950–1960 (2018).
11. Kraft, A. Some considerations on the structure, composition, and properties of Prussian blue: a contribution to the current discussion. *Ionics* **27**, 2289–2305 (2021).
12. Ivanov, V. D. Four decades of electrochemical investigation of Prussian blue. *Ionics* **26**, 531–547 (2020).
13. Ma, L. et al. Accommodating diverse ions in Prussian blue analogs frameworks for rechargeable batteries: the electrochemical redox reactions. *Nano Energy* **81**, 105632 (2021).
14. Li, W. J. et al. Chemical properties, structural properties, and energy storage applications of Prussian blue analogues. *Small* **15**, 1900470 (2019).
15. Buser, H. J., Schwarzenbach, D., Petter, W. & Ludi, A. The crystal structure of Prussian blue: Fe₄[Fe(CN)₆]₃·xH₂O. *Inorg. Chem.* **16**, 2704–2710 (1977).
16. Lu, Y., Wang, L., Cheng, J. & Goodenough, J. B. Prussian blue: a new framework of electrode materials for sodium batteries. *Chem. Commun.* **48**, 6544–6546 (2012).

17. Zhang, L., Chen, L., Zhou, X. & Liu, Z. Towards high-voltage aqueous metal-ion batteries beyond 1.5 V: the zinc/zinc hexacyanoferrate system. *Adv. Energy Mater.* **5**, 1400930 (2015).
18. Lee, H. W., Pasta, M., Wang, R. Y., Ruffo, R. & Cui, Y. Effect of the alkali insertion ion on the electrochemical properties of nickel hexacyanoferrate electrodes. *Faraday Discuss.* **176**, 69–81 (2014).
19. Kim, D.-M. et al. Co-intercalation of Mg^{2+} and Na^+ in $Na_{0.69}Fe_2(CN)_6$ as a high-voltage cathode for magnesium batteries. *ACS Appl. Mater. Interfaces* **8**, 8554–8560 (2016).
20. Liu, Y. et al. Sodium storage in Na-rich $Na_xFeFe(CN)_6$ nanocubes. *Nano Energy* **12**, 386–393 (2015).
21. Li, W. J. et al. Facile method to synthesize Na-enriched $Na_{1+x}FeFe(CN)_6$ frameworks as cathode with superior electrochemical performance for sodium-ion batteries. *Chem. Mater.* **27**, 1997–2003 (2015).
22. You, Y., Yu, X., Yin, Y., Nam, K.-W. & Guo, Y. G. Sodium iron hexacyanoferrate with high Na content as a Na-rich cathode material for Na-ion batteries. *Nano Res.* **8**, 117–128 (2015).
23. Xiao, P., Song, J., Wang, L., Goodenough, J. B. & Henkelman, G. Theoretical study of the structural evolution of a $Na_2FeMn(CN)_6$ cathode upon Na intercalation. *Chem. Mater.* **27**, 3763–3768 (2015).
24. Ling, C., Chen, J. & Mizuno, F. First-principles study of alkali and alkaline earth ion intercalation in iron hexacyanoferrate: the important role of ionic radius. *J. Phys. Chem. C* **117**, 21158–21165 (2013).
25. Imanishi, N. et al. Lithium intercalation behavior into iron cyanide complex as positive electrode of lithium secondary battery. *J. Power Sources* **79**, 215–219 (1999).
26. Asakura, D. et al. Fabrication of a cyanide-bridged coordination polymer electrode for enhanced electrochemical ion storage ability. *J. Phys. Chem. C* **116**, 8364–8369 (2012).
27. Shen, L., Wang, Z. & Chen, L. Prussian blues as a cathode material for lithium ion batteries. *Chem. Eur. J.* **20**, 12559–12562 (2014).
28. Wu, X. et al. Low defect $FeFe(CN)_6$ framework as stable host material for high performance Li-ion batteries. *ACS Appl. Mater. Interfaces* **8**, 23706–23712 (2016).
29. Wang, B. et al. Gradient substitution: an intrinsic strategy towards high performance sodium storage in Prussian blue-based cathodes. *J. Mater. Chem. A* **6**, 8947–8954 (2018).
30. Tang, X. et al. Hierarchical sodium-rich Prussian blue hollow nanospheres as high-performance cathode for sodium-ion batteries. *Nano Res.* **11**, 3979–3990 (2018).
31. Liu, Y. et al. A heterostructure coupling of bioinspired, adhesive polydopamine, and porous Prussian blue nanocubics as cathode for high-performance sodium-ion battery. *Small* **16**, 1906946 (2020).
32. Wang, B. et al. Prussian blue analogs for rechargeable batteries. *iScience* **3**, 110–133 (2018).
33. Herren, F., Fischer, P., Ludi, A. & Haelg, W. Neutron diffraction study of Prussian Blue, $Fe_4[Fe(CN)_6]_3 \cdot xH_2O$. Location of water molecules and long-range magnetic order. *Inorg. Chem.* **19**, 956–959 (1980).
34. Kumar, A., Yusuf, S. M. & Keller, L. Structural and magnetic properties of $Fe_4[Fe(CN)_6]_3 \cdot 4H_2O$. *Phys. Rev. B* **71**, 054414 (2005).
35. Takachi, M., Fukuzumi, Y. & Moritomo, Y. Na^+ diffusion kinetics in nanoporous metal-hexacyanoferrates. *Dalton Trans.* **45**, 458–461 (2016).
36. Yu, Z. Y. et al. Unconventional CN vacancies suppress iron-leaching in Prussian blue analogue pre-catalyst for boosted oxygen evolution catalysis. *Nat. Commun.* **10**, 2799 (2019).
37. Pérez-Ramírez, J. et al. Evolution of isomorphously substituted iron zeolites during activation: comparison of Fe-beta and Fe-ZSM-5. *J. Catal.* **232**, 318–334 (2005).
38. Dzwigaj, S., Stievano, L., Wagner, F. E. & Che, M. Effect of preparation and metal content on the introduction of Fe in BEA zeolite, studied by DR UV-vis, EPR and Mössbauer spectroscopy. *J. Phys. Chem. Solids* **68**, 1885–1891 (2007).
39. Chong, S. et al. Potassium nickel iron hexacyanoferrate as ultra-long-life cathode material for potassium-ion batteries with high energy density. *ACS Nano* **14**, 9807–9818 (2020).
40. Zhang, C. et al. Potassium Prussian blue nanoparticles: a low-cost cathode material for potassium-ion batteries. *Adv. Funct. Mater.* **27**, 1604307 (2017).
41. He, X. et al. A novel highly crystalline $Fe_4(Fe(CN)_6)_3$ concave cube anode material for Li-ion batteries with high capacity and long life. *J. Mater. Chem. A* **7**, 11478–11486 (2019).
42. Huang, Y. et al. A novel border-rich Prussian blue synthesized by inhibitor control as cathode for sodium ion batteries. *Nano Energy* **39**, 273–283 (2017).
43. Pajeroski, D. M., Watanabe, T., Yamamoto, T. & Einaga, Y. Electronic conductivity in berlin green and Prussian blue. *Phys. Rev. B* **83**, 153202 (2011).
44. Qian, J., Zhou, M., Cao, Y., Ai, X. & Yang, H. Nanosized $Na_4Fe(CN)_6/C$ composite as a low-cost and high-rate cathode material for sodium-ion batteries. *Adv. Energy Mater.* **2**, 410–414 (2012).
45. Ma, Y. et al. High-entropy metal-organic frameworks for highly reversible sodium storage. *Adv. Mater.* **33**, 2101342 (2021).
46. Griffith, D. W. T. & Galle, B. Flux measurements of NH_3 , N_2O and CO_2 using dual beam FTIR spectroscopy and the flux-gradient technique. *Atmos. Environ.* **34**, 1087–1098 (2000).
47. Shang, Y. et al. Unconventional Mn vacancies in Mn-Fe Prussian blue analogs: suppressing Jahn-Teller distortion for ultrastable sodium storage. *Chem* **6**, 1804–1818 (2020).
48. He, G. & Nazar, L. F. Crystallite size control of Prussian white analogues for nonaqueous potassium-ion batteries. *ACS Energy Lett.* **2**, 1122–1127 (2017).
49. You, Y. et al. Subzero-temperature cathode for a sodium-ion battery. *Adv. Mater.* **28**, 7243–7248 (2016).
50. Wang, W. et al. Reversible structural evolution of sodium-rich rhombohedral Prussian blue for sodium-ion batteries. *Nat. Commun.* **11**, 980 (2020).
51. Guo, X. et al. Water contributes to higher energy density and cycling stability of Prussian blue analogue cathodes for aqueous sodium-ion batteries. *Chem. Mater.* **31**, 5933–5942 (2019).
52. Peng, J. et al. Defect-free-induced Na^+ disordering in electrode materials. *Energy Environ. Sci.* **14**, 3130–3140 (2021).
53. He, G., Huq, A., Kan, W. H. & Manthiram, A. β - $NaVOPO_4$ obtained by a low-temperature synthesis process: a new 3.3 V cathode for sodium-ion batteries. *Chem. Mater.* **28**, 1503–1512 (2016).
54. Zhang, Z. H., Ni, Y., Avdeev, M., Kan, W. H. & He, G. Dual-ion intercalation to enable high-capacity $VOPO_4$ cathodes for Na-ion batteries. *Electrochim. Acta* **365**, 137376 (2021).
55. You, Y., Wu, X. L., Yin, Y. X. & Guo, Y. G. High-quality Prussian blue crystals as superior cathode materials for room-temperature sodium-ion batteries. *Energy Environ. Sci.* **7**, 1643–1647 (2014).
56. Wu, X. et al. Single-crystal $FeFe(CN)_6$ nanoparticles: a high capacity and high rate cathode for Na-ion batteries. *J. Mater. Chem. A* **1**, 10130–10134 (2013).
57. Wang, L. et al. A superior low-cost cathode for a Na-ion battery. *Angew. Chem. Int. Ed.* **52**, 1964–1967 (2013).
58. Mandal, B., Basumallick, I. & Ghosh, S. Synthesis, characterization and electrochemical studies on $Li_4Fe(CN)_6$ as cathode material for lithium batteries. *J. Pure Appl. Chem.* **5**, 30–42 (2015).
59. Mandal, B. A novel aqueous $Li_4Fe(CN)_6$ cathode and hydrophobic ionic liquid electrolyte combined lithium-ion battery. *Adv. Mater. Proc.* **2**, 745–748 (2017).
60. Toby, B. H. EXPGUI, a graphical user interface for GSAS. *J. Appl. Crystallogr.* **34**, 210–213 (2001).

Acknowledgements

This work was supported by the National Key Research and Development Program of China (2019YFA0205700), the National Natural Science Foundation of China (51602219); Tianjin Municipal Science and Technology Commission (No. 17JCYBJC42000); W.H.K. acknowledges the National Natural Science Foundation of China (11805034, 21704105, and U1930102), and the Natural Science Foundation of Guangdong Province (2017A030313021). The authors gratefully acknowledge the beamtime in ECHIDNA granted from Australian Centre for Neutron Scattering (ACNS) in ANSTO.

Author contributions

G.H. and Z.Z. conceived the idea and designed the experiments. Z.Z. conducted the characterizations, performed the electrochemical measurements, analyzed the results, and drafted the manuscript. H.C. and W.Y. performed the powder neutron diffraction for materials. M.A. provided comments on the manuscript. W.H.K. contributed to the theoretical calculations and analyses of powder neutron diffraction for materials. G.H. proposed the research, revised the manuscript and supervised this work. All the authors contributed to the interpretation of the results.

Competing interests

The authors declare no competing interests.

Additional information

Supplementary information The online version contains supplementary material available at <https://doi.org/10.1038/s41467-022-35376-1>.

Correspondence and requests for materials should be addressed to Wang Hay Kan or Guang He.

Peer review information *Nature Communications* thanks Swastika Banerjee, Vilas Pol, and the other, anonymous, reviewer(s) for their contribution to the peer review of this work.

Reprints and permissions information is available at <http://www.nature.com/reprints>

Publisher's note Springer Nature remains neutral with regard to jurisdictional claims in published maps and institutional affiliations.

Open Access This article is licensed under a Creative Commons Attribution 4.0 International License, which permits use, sharing, adaptation, distribution and reproduction in any medium or format, as long as you give appropriate credit to the original author(s) and the source, provide a link to the Creative Commons license, and indicate if changes were made. The images or other third party material in this article are included in the article's Creative Commons license, unless indicated otherwise in a credit line to the material. If material is not included in the article's Creative Commons license and your intended use is not permitted by statutory regulation or exceeds the permitted use, you will need to obtain permission directly from the copyright holder. To view a copy of this license, visit <http://creativecommons.org/licenses/by/4.0/>.

© The Author(s) 2022